Developing an Angular Correlation Measurement of Undulator Radiation from a Single Electron in the IOTA Facility

Evan Angelico, Sergei Nagaitsev, Giulio Stancari

The properties of radiation emitted when a single electron passes through an undulator element, though quantum in nature due to small occupation number, should extrapolate to the same observed properties of undulator radiation in the high occupation number of an intense electron beam. A measurement of the angular distribution of radiation from a single electron is being developed at the Integrable Optics Test Accelerator (IOTA) facility under the experimental name AMPUR, described in this document. One feature of undulator radiation from a single electron is that during a single accelerator period, there is a non-negligable chance that two photoelectrons are generated in a detector viewing the radiation region. The system described in this document is designed to measure the angle between these two photoelectrons relative to the trajectory of the circulating electron. Micro-channel plate based photomultipliers are considered as a candidate detector technology, and a small detector has been used to measure undulator radiation in the Run 2b phase of IOTA. The considerations for a next phase of this measurement are detailed, possibly involving the use of Large Area Picosecond Photodetectors.

CONTENTS

ACKNOWLEDGMENTS

I. INTRODUCTION

The properties of radiation emitted when a single electron passes through an undulator element, though quantum in nature due to small occupation number, should extrapolate to the same observed properties of undulator radiation in the high occupation number of an intense electron beam. One phenomenon that emerges when considering the electron's interaction with the undulator field in quantum electrodynamics (QED) is a non-negligable probability of two photoelectrons being generated in a detector viewing the radiation during a single passing of the electron through the undulator.

This document describes the development of a measurement of the angle of the position of those photo-

electrons with respect to the axis of the particle trajectory. One goal of the measurement is to confirm that the angular distribution of undulator radiation from a single electron matches the distribution expected from an intense beam. Additionally, the precision measurement of undulator radiation at the single photon level may provide instrumentation useful for other undulator-based beam systems such as those used for optical stochastic cooling or self-amplified spontaneous emission.

Section I reviews background information on undulator radiation, and introduces the measurement of the angular distribution. Requirements and detector specifications for this measurement are also described. Section II describes the experimental apparatus used for the AMPUR experiment, a first-phase measurement of single photons from undulator radiation in the IOTA facility during Run 2b. This section includes details about the detector and the data acquisition system installed. Section III describes the data that was taken during that experimental run. Section V reflects on the experiences of Run 2b to form a set of pathways for the next phase of this measurement, possibly involving Large Area Picosecond Photodetectors (LAPPDs) or multiple small microchannel plate photomultipliers. Finally, Section VI goes through the details of the analysis procedure used to explore data from Run 2b of AMPUR.

A. Undulator radiation from a single electron

Synchrotron radiation emitted from a bunch of electrons passing through an undulator has a roughly conical angular divergence related to the relativistic parameter γ of the beam, the strength parameter K of the undulator, and the wavelength and number of periods of the undulator dipoles [13]. The angular and spectral density may be decomposed into a harmonic structure containing a squared difference of $\frac{n-1}{2}$ and $\frac{n+1}{2}$ order Bessel functions with their argument related only to the undulator strength parameter, number of periods, and the period of the undulator [9, 13]. The resulting spectral and angular distributions are shown in the next subsection for the case specific to this experiment in the IOTA facility.

When only a single electron passes through the undulator, one can consider the effect of quantum fluctuations in the radiation process by taking into account higher order interactions in quantum electrodynamics (QED)[12]. The solutions to the Lagrangian for a strong external electromagnetic field (undulator) interacting with an electron are Dirac-Volkov states dressed by the strong field [8]. The resulting final states are states of the radiation field, i.e. a superposition of all photon number states; when detected by a photodetector, this coherent radiation state collapses to a number state, for example the number of photoelectrons in a photodetector [6, 19].

Another perspective, using the tools provided by Feynman diagrams, describes this radiation process as an infinite sum of interactions of the electron with the photons in the undulator field, each term containing a higher order interaction in the perturbation series. Single photon emission may be represented by a one vertex Feynman diagram representing Compton scattering between the electron and the undulator field. The next-to-leading order diagrams include the emission of two incoherent photons, emitted from a different space-time region, or two coherent photons, emitted from the same space-time region [8]. In one pass of the electron through the undulator field, a resulting final state is two photons later detected by a downstream photodetector.

In the remainder of this document, the angular measurement is sometimes described as a measurement of the angle of two photons emitted during the passing through the undulator, even though in the radiation-field perspective the undulator radiation does not become a number state until it is measured and converted into two photoelectrons at the detector.

B. Undulator radiation in the Integrable Optics Test Accelerator

FIG. 1. The SLAC STI Optronics undulator installed in IOTA. This undulator has a K parameter of 1.0 and 10 periods at 55 mm wavelength (see Reference [17]).

The Integrable Optics Test Accelerator (IOTA) is a storage ring at Fermi National Accelerator Laboratory (Fermilab) with a research program that includes studying nonlinear focusing integrable-optical beam lattices, beam dynamics of space-charge effects, optical stochastic cooling, and more [5]. An STI Optronics undulator provided by the Stanford Linear Accelerator Center (SLAC) was installed into one of the nonlinear-optics insertion stations in IOTA in 2018-2019. This undulator, photograph shown in Figure 1, will be used to measure properties of undulator radiation as well as to test methods of optical-stochastic beam cooling.

In the second run period of IOTA, Run 2, four bunches of 100 MeV electrons circulate the 40 m circumference with 7.5 MHz cycle frequency (133 ns cyle period, harmonic number 4). The IOTA facility had the ability to run at a max average current of about 3.5 mA, as well as circulate a single electron with a maximum lifetime on the order of 2 hours. The undulator used has strength parameter K of 1.0, a period of 55 mm, and 10 periods resulting in a first harmonic emission wavelength of 1077 nm [17, 20].

The differential emission rate per turn of a single electron as a function of synchrotron wavelength is shown in light red in Figure 2. The other lines on this plot are related to the detector instrumentation discussed in the next section. The angular differential-emission spectrum is shown on the left-hand side of Figure 3. These quantities are calculated using the python wigrad package maintained by Ihar Lobach [18].
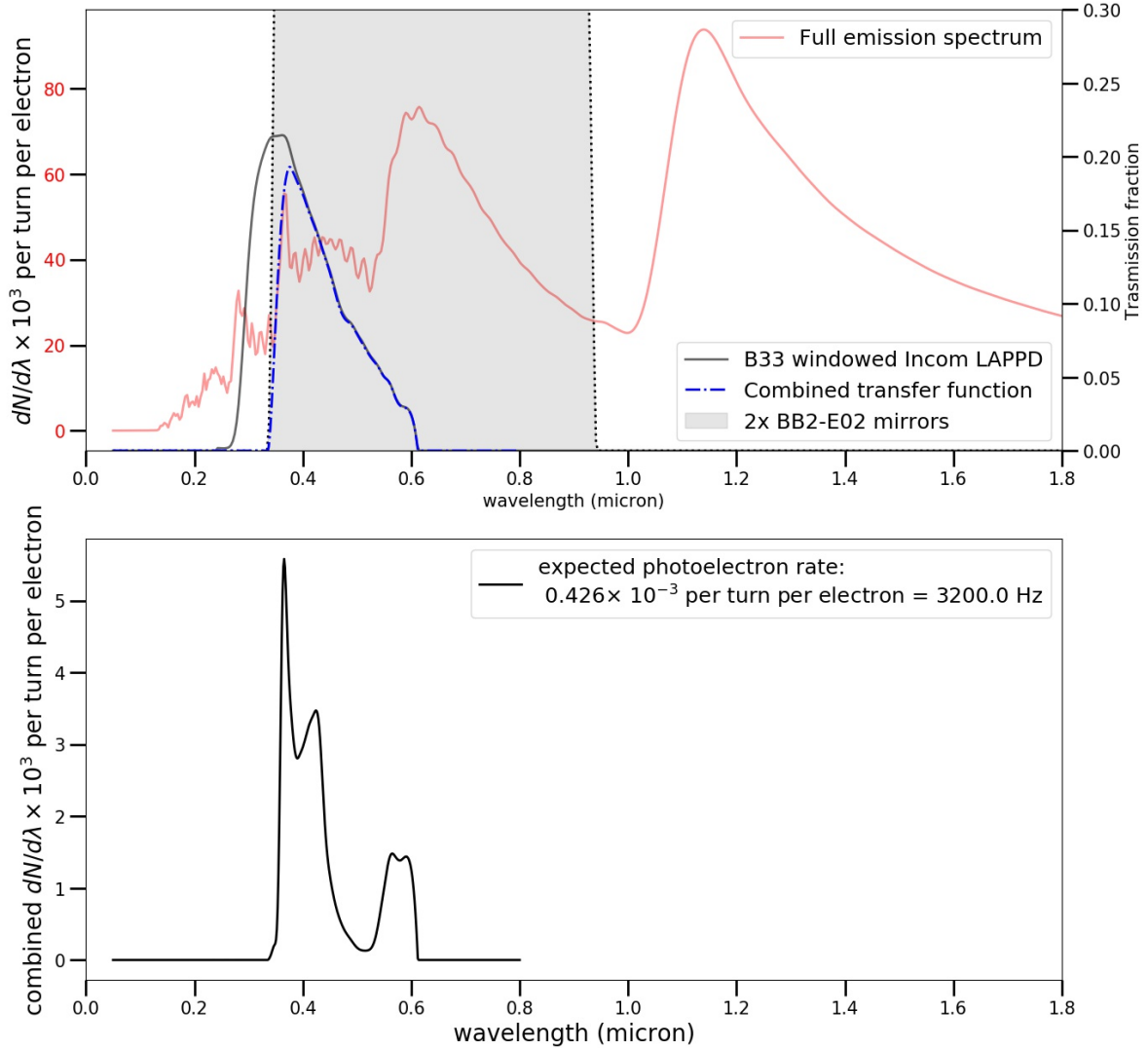
FIG. 2. Top: in light red, the full simulated emission spectrum integrated over all emission angles, calculated using code in Reference [18] with parameters matching the SLAC STI Optronics undulator installed in IOTA. The fundamental of this undulator is at 1077 nm, but by summing over all of angular space, as is done in the red trace, the peak shifts to 1140 nm. This simulation includes light emitted up to 180 mrad, 8 harmonics, and a Bessel harmonic cutoff of 15. In black shade, the reflectance of two BB2-E02 [38] mirrors used to direct light to the detector, which has close to 100% reflection in the shaded region. In black line, the quantum efficiency of an Incom LAPPD with B33 [32] window and bi-alkali photocathode typical in MCP-PMTs. In blue, the combination of mirrors, quantum efficiency, and detector window transmission. Bottom: the combined detected photoelectron spectrum whose integral represents about 3200 Hz per electron for a 7.5 MHz cycle frequency.

C.   Specifications for an angular correlation measurement

The critical specifications of a detector system that is able to measure the two-photon angular correlation are:

1. The ability to detect single photons in the optical to infrared spectral region with efficiency higher than about 10 %.

FIG. 3. Angular distribution integrated over wavelength of the simulated undulator emission with parameters matching the SLAC STI Optronics undulator installed in IOTA. The black outline re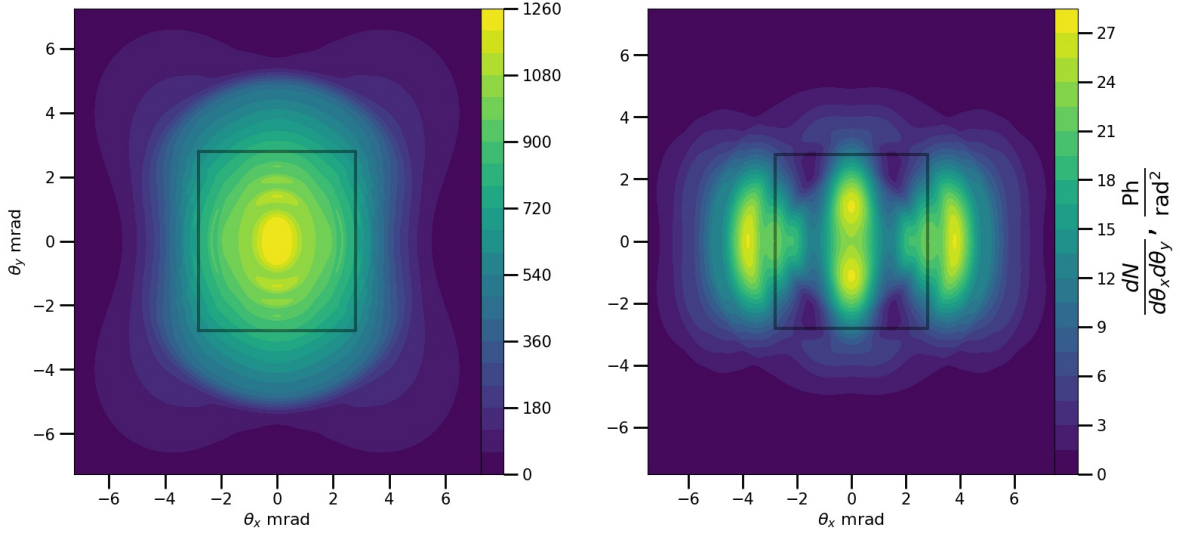presents the boundaries of a 2 cm detector at a distance 3.5 m from the emission location. Both plots are a sum of both linear polarities. Left: wavelength range from 200 - 1800 nm. Right: spectrum convoluted with the mirror reflectivity, detector quantum efficiency, and detector window transmission. The angular distribution of the harmonics follows the "squared-difference of Bessel functions" described in Reference [9] and are simulated using code in Reference [18].

2. The ability to detect and distinguish two photons that arrive at the same or different regions in space within a 10 ns time period. Note, this means both distinguishing whether a detection represents 1 photon or 2 photons and, if the detection corresponds to 2 photons, the positions of those two photons regardless if they are completely overlapping in space or spatially separated.

3. Have a large ratio between the active photodetector length and 2D photon-position resolution, which corresponds to a fine angle-difference resolution.

4. The ability to read and refresh the signal digitization buffer on a timescale that is no longer than the expected arrival of photons, which is on the order of 100 μs corresponding to the $\simeq$ 3 - 10 kHz expected signal event rate assuming 20-30% quantum efficiency (see Figure 2).

5. Have low enough dark-noise rate such that a 10 ns gated readout over a 133 ns electron cycling period has a small noise acceptance compared to 10 kHz single photon and 10 Hz double photon detection rates.

1. Micro-channel plate photomultplier tubes

Microchannel plates (MCPs) are a single-electron amplification technology, reviewed in detail in Reference [39]. A glass substrate is fabricated with many closely-packed pores having diameters on the order of 10s of μm and lengths on the order of 1 mm. The insides of the pores are coated with a secondary emitting material. With modern fabrication techniques using atomic layer deposition, amplification factors, or gains, of 10^7 are typical when placing two MCPs in succession with a gap in between, called the "Chevron" configuration [21, 39]. The high gain-bandwidth and thin geometry of microchannel plates is what allows MCP-PMTs to achieve 20 - 70 picoseconds timing resolutions on single photons. For more information regarding the operating principle of MCP-PMTs, see Reference [4].
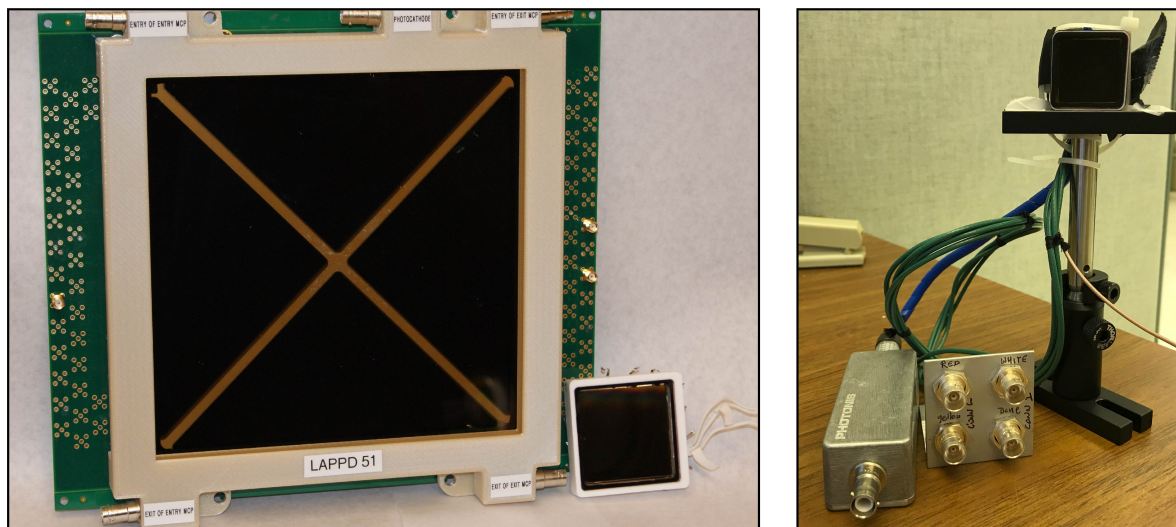
FIG. 4. Left: photograph of a Large Area Picosecond Photodetector fabricated by Incom Inc. and a 5 cm Photonis Planacon. Right: photograph of the 2 cm Planacon used in this phase of the AMPUR experiment.

Microchannel plates decouple the spatial resolution and the size of the sensitive area in an MCP-based detector. Their spatial resolutions are in principle limited by the size of the MCP pores ($\simeq$ 5 - 25 μm) but in practice are limited by the geometry of the detector and its readout. Some readout geometries have demonstrated less than 25 μm spatial resolution [36] and other geometries result in 500 - 1000 μm resolutions [2, 7].

Advancements in MCP fabrication that move away from lead-glass MCP substrates have made it possible to produce MCP-PMTs with 400 cm^2 sensitive area [1]. These same advancements in MCP fabrication have allowed MCP-PMTs with bialkali photocathodes to achieve dark-noise rates on the order of 100 Hz / cm^2.

Microchannel plate based detectors have the ability to distinguish between one and two photoelectrons due to their high single-photoelectron amplification. An example of single-photoelectron separation is shown in Figure 6 in the next section.

For a measurement of the angle of single photoelectrons generated by viewing undulator radiation, the readout geometry and the size of the detector are important experiment design considerations. These two qualities constrain the design of the readout electronics system, including the trigger and digitization flow, as well as the resulting angular correlation sensitivity.

2. *Semiconductor-based photo-detectors*

One example of a commonly used semiconductor based photo-detector is a silicon photo-multiplier (SiPM) which typically is configured as a pixellated array of single-photon avalanche diodes (SPAD). SiPMs have unprecedented sensitivity to distinguishing the number of photoelectrons detected and also have detection efficiencies of greater than 20% in the optical region.

The SiPM pixel size is roughly equal to its spatial resolution, typically on the order of 0.5 - 10 mm. To achieve sensitive detector length to position resolution ratios comparable to commercially available MCP-PMTs, one would require on order 1,000 - 18,000 SiPM electronics channels.

The dark-noise rate of SiPM pixels at room temperature varies but is on the order of 1 MHz / cm^2 or higher [34]. The dark-rate is drastically reduced at low temperatures, for example to less than 5 kHz / cm^2 at

165 Kelvin [26]. Without additional supporting design factors, high dark-noise rate is the main quality that disqualifies SiPMs as a detector technology for this angular measurement.

II. EXPERIMENTAL SETUP
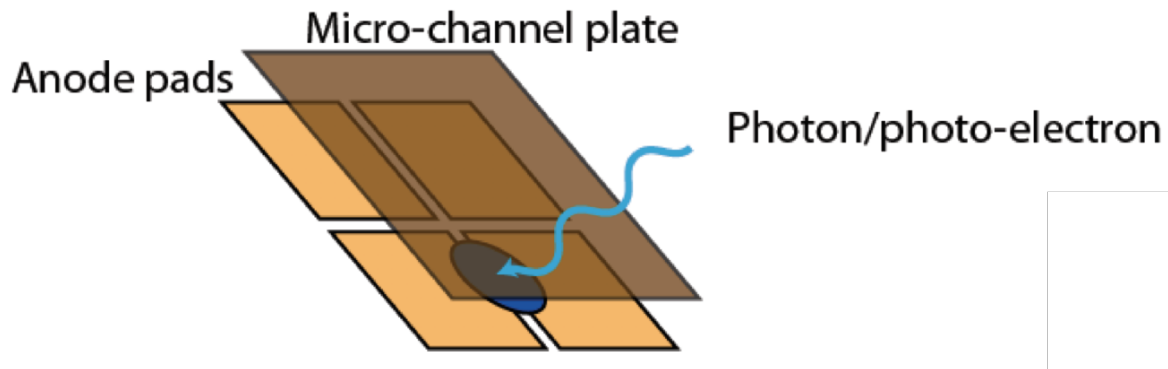
A. Detector configuration

FIG. 5. An illustration of the signal-sharing between multiple pads in the four-pad anode of the Planacon used in AMPUR. The microchannel plates produce a macroscopic charge cloud that induces signals in anode pads. In the case of one photoelectron, the incident position may be reconstructed using the fractional signal sharing of each pad. In the case of two photoelectrons and the large anode pads of this four-pad Planacon, the position and fractional-signal distribution become mixed measureables.

A test of the candidate MCP-PMT technology, a small-format MCP-PMT from Photonis called the mini-Planacon XPM85112 [29] was instrumented into the beam to detect two-photon emission from a single electron, shown in Figure 4. A system of lens-tubes coupled to a viewport downstream of the undulator reflects undulator radiation off of optical mirrors, directing the undulator radiation cone to a dark box situated above the accelerating structure. The total optical-path length from the center of the undulator to the dark box is about 3.5 meters. The 2 cm side-length of the Planacon correpsonds to a half-angle acceptance of 2.86 mrad.

The readout of the XPM85112 is a 4 x 4 array of square pads internal to the detector vacuum packaging. Externally, the 4 x 4 array is converted to a 2 x 2 array by connecting adjacent pads. This connection is made using hookup wire close to the 2 x 16 signal-pin headers on the back of the detector.

Charge clouds produced by the microchannel plates induce a voltage in a single anode pad or multiple anode pads depending on the position of the primary electron and the size of the charge cloud. This signal-sharing property of MCP-PMT readouts, illustrated in Figure 5, allows for continuous position resolution across the photosensitive area, and also allows for better position resolution than the size of the anode pad [27].

Depending on the size of the anode pads relative to the charge-cloud size, the signal-sharing property can negatively affect one's ability to distinguish the positions of two photons. For example, two photoelectrons that produce a lower-than-average amplitude pulse and that land at the center of two adjacent anode pads may look like one photoelectron arriving directly between the two anode pads. For this reason, it is advantageous to have anode pads that are much smaller than the expected separation distances of the photons (see Specification 2). This challenge may be overcome by calibrating the 2D position response and single photoelectron response as described later in Section V.

1. Typical quantum efficiency

The quantum efficiency of this detector was not characterized during Run 2b and represents a possible source of systematic uncertainty. The mini-Planacon XPM85112 has a typical quantum efficiency of 22% peaking at 380 nm as shown in its datasheet in Reference [28]. The spectrum of the LAPPD quantum efficiency shown in Figure 2 is similar to the reported spectrum in the XPM 85112 datasheet. The reflectance spectrum of the two ThorLabs BB2-E02 mirrors [38] is shown in shaded grey, and the resulting detection spectrum is shown in blue. The mirrors are the element that rejects the most ultra-violet light. The resulting differential detection rate per single electron per pass through the undulator is displayed in the lower subfigure. Integrating this spectrum results in about 0.426×10^{-3} photoelectrons detected by the Planacon per turn per electron. For a 133 ns IOTA period, this corresponds to a rate of about 3200 Hz of single photoelectron detections.

2. Gain
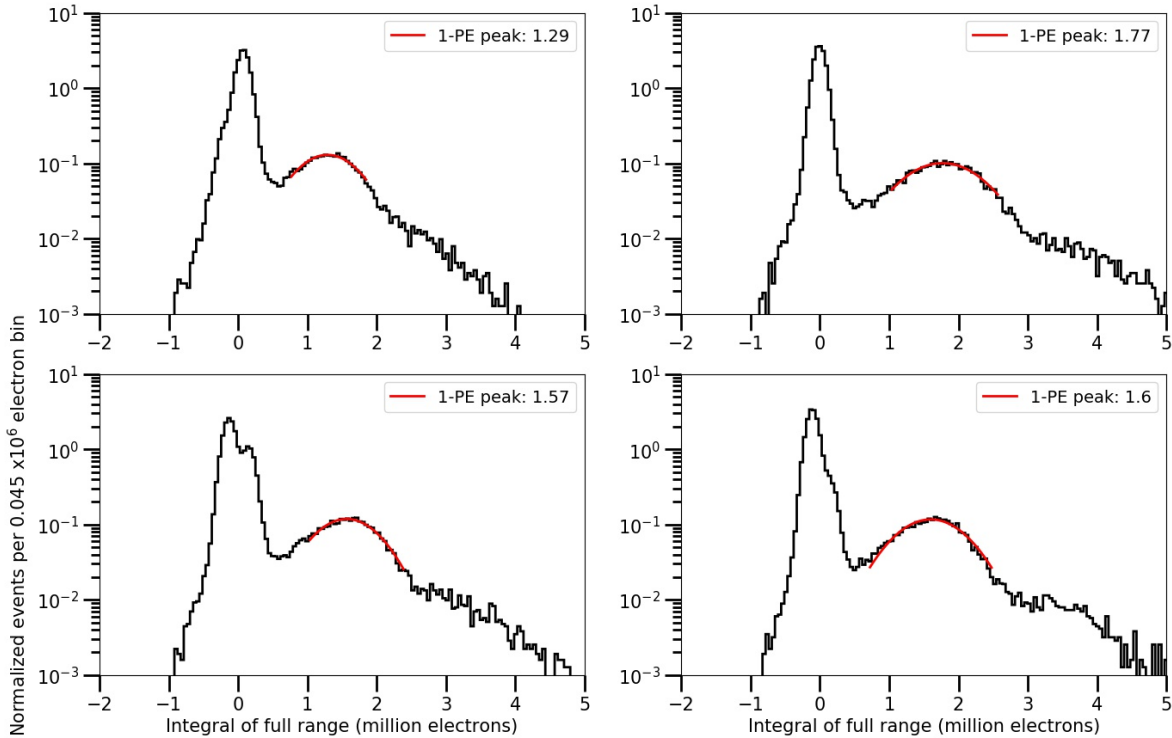
FIG. 6. Single photoelectron charge spectrum using an attenuated pulsed laser with 2400 V applied to the detector high-voltage input. The laser is aligned with the center of each anode pad and 70k events are recorded at an occupancy of about 0.2 photoelectrons per pulse. Each sub-plot represents the spectrum for that pad, with the subplots oriented in the light-cone's "beam's-eye view".

The gain of the mini-Planacon with the high-voltage divider provided by Photonis has been tested by Photonis prior to sale [30]. If one assumes that the gain function has the following form,

$$\log_{10}(G) = mV + b \tag{1}$$
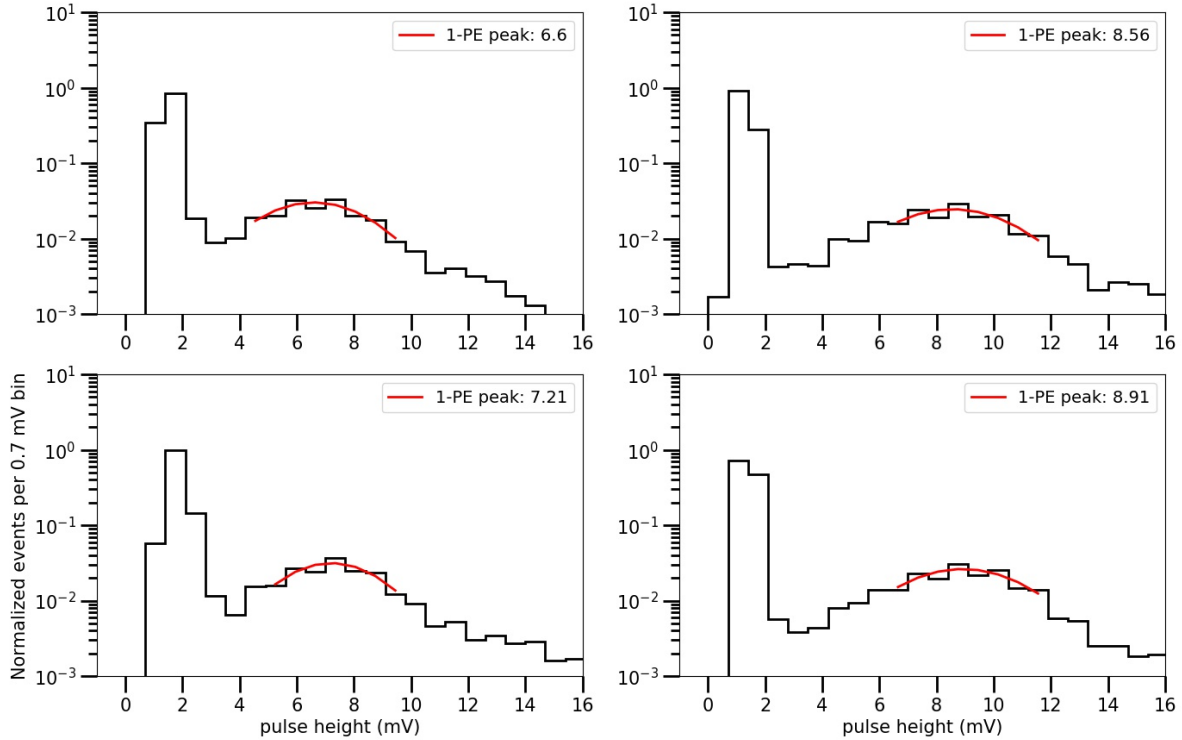
FIG. 7. Single photoelectron pulse-height distribution using the same data as in Figure 6. Pulse heights are defined as the minimum sample within the digitized event waveform, as the pulses are negative polar. This histogram has an applied factor of -1.

where V is the voltage applied to the input of the provided high-voltage divider associated with this detector, and G is the gain, then the parameters based on the test sheet correspond to $m = 0.0033$ V^{-1}, and $b = -1.532$.

During the experimental phase, two high voltage settings were used: 2400 V and 2480 V corresponding to 2.4×10^6 and 4.5×10^6 gain respectively using the relation above. The gain at 2400 V was calibrated using a Tektronix DPO7354 and a pulsed laser attenuated to produce a detector occupancy of about 0.2 pulses per laser trigger. Pulses were measured at the center of each anode pad. The 70k events were integrated over at 10 ns range containing the expected single photoelectron pulses.

The resulting charge spectrum results in a gain of 1.3 to 1.77×10^6 depending on the channel, shown in Figure 6. The pulse heights are also extracted without a noise threshold, resulting in a peak pulse height of 6.6 to 8.91 mV as shown in Figure 7.

B. Data acquisition system

The data acquisition system (DAQ) is shown in diagram form in Figure 8. The Planacon was installed in the dark-box station above the M4R IOTA bending magnet. Light is directed onto the surface of the Planacon without the use of lenses, resulting in an expected angular distribution of photons inside the black square of Figure 3. The anode pads are coupled to four RG58 BNC cables which exit the dark box. These signal cables are connected to 75 m RG58 BNC cables that route from the IOTA cavern to the Electronics Service Building (ESB) at ground level.
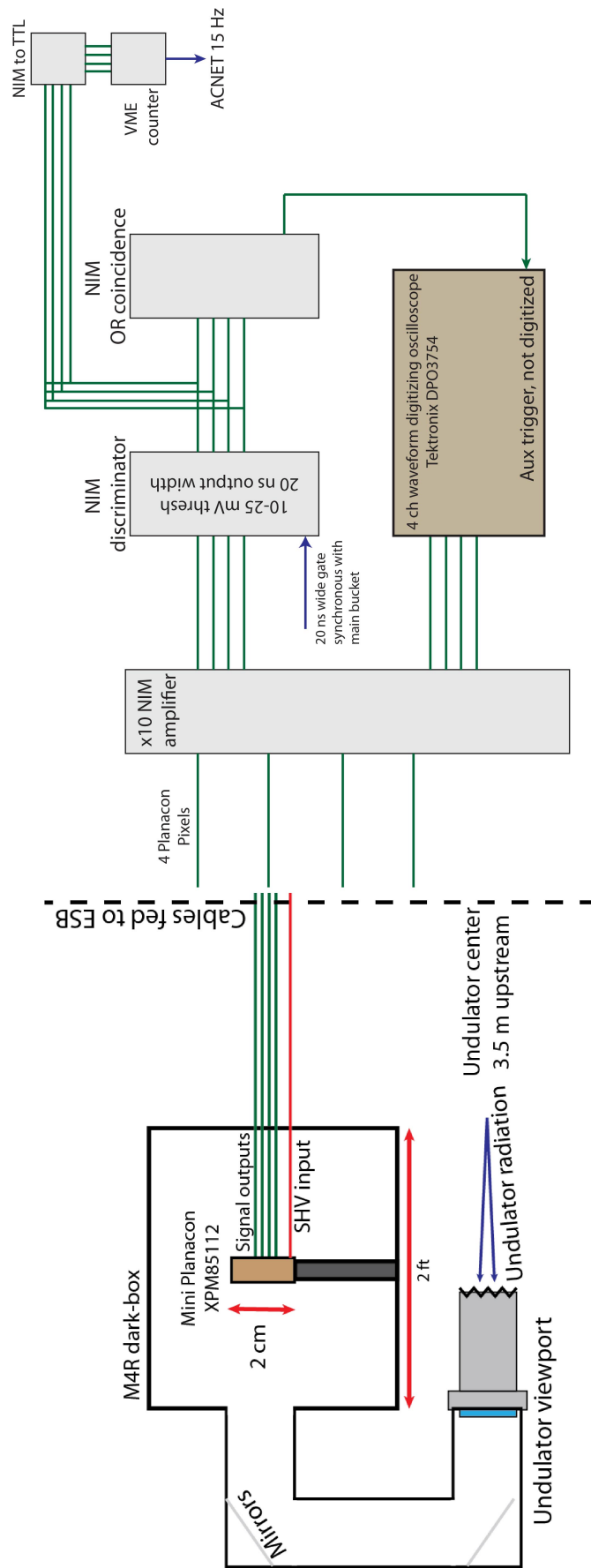
FIG. 8. Undulator radiation is directed to the Planacon via motor controlled mirror mounts inside of a lens tube system. The Planacon is aligned with the beam in one dimension using a translation stage directed into the page. Photoelectrons produce pulses that are sent to an upstairs DAQ room over 75 m of RG58 coax cable. Signals are amplified by an AC coupled 20 dB NIM amplifier with two outputs per input channel. One output of the amplifier is sent to a digitizing Tektronix DPO7354 oscilloscope. The second output is discriminated by a NIM discriminator whose inputs are gated by a 20 ns window aligned with the 7.5 MHz RF clock. Discriminator outputs are routed to (1) a VME counter on each channel and (2) a coincidence logic unit configured as a four-way OR gate. The output of the logic gate is used to trigger the oscilloscope and is not digitized

Due to technical difficulties, the signals exiting the dark box were not pre-amplified. Instead, the signals are amplified by a 20 dB AC-coupled NIM amplifier in ESB. The losses in 75 m of RG58 cable in the frequency range of 200 to 500 MHz is about -20 dB [31]. The low gain of the MCPs in combination with a net gain of 0 dB through the DAQ chain results in a poor separation between single photoelectron amplitude and minimum discriminator threshold of about -15 mV [22]

The routing of signal lines after amplification by the NIM amplifier is shown on the right-hand side of Figure 8. One output of the two-channel amplifier is sent to a digitizing Tektronix DPO7354 oscilloscope. The second output is discriminated by a NIM discriminator whose inputs are gated by a 20 ns window aligned with the 7.5 MHz RF clock as well as the passage of the electron through the undulator. Discriminator outputs are routed to (1) a VME counter on each channel and (2) a coincidence logic unit configured as a summed OR gate. The output of the OR coincidence is used to trigger the oscilloscope but is not digitized by the oscilloscope.

The result is a DAQ system that digitizes a 100 ns event containing all four channels whenever 1 or more of the amplified signals goes above threshold within the 20 ns gate, which is aligned with the arrival of the electron at the undulator. Those events are stored to an external hard drive in 9000-event batches. An additional handle on the state of the detector comes from the live-monitored VME counters that increment whenever the channel goes above threshold during the 20 ns gate. The VME counters are routed to ACNET variables NISRCNT 11, 12, 13, and 14 corresponding to channels 1, 2, 3, and 4.

III. DATA COLLECTION DURING RUN 2B

Six 8 hour shifts were taken during IOTA Run 2b in the time period between 2/26 and 3/18 of 2020. The details of each shift summary may be found at the AMPUR experiment redmine wiki: hyperlink here. The first few shifts were used to measure photons from many electrons circulating the ring, align the detector with the emission cone from the undulator, confirm expected rates, tune the timing of the DAQ gate, determine minimum discriminator thresholds, and develop the procedure for producing a single circulating electron in IOTA based on procedures developed during Run 1. The shifts on 3/3, 3/5, and 3/8 produced data useful for single electron analyses summarized later in Table I.

A. Beam configuration

The mini-Planacon is mounted on a translation stage that shifts it into and out of the optical path of undulator emission. The position parallel to the optical path is fixed. On 3/3, the detector position was scanned incrementally out of the radiation cone as shown in Figure 9. This figure shows the VME counter rates over time, where the position of the detector is incremented every few minutes. The variation in the detection rates are due to slight variations in the discriminator thresholds, as well as variations in the gain for each channel, amplification factor from the NIM amplifier, and angular distribution of emitted light. The operating position is chosen to maximize both rate and channel-rate uniformity.

On 3/5, the rate of the discriminator channels are monitored as the IOTA beam is scraped, reducing the number of circulating electrons from 100 s to one. Figure 10 shows the rate of each channel averaged over 3 seconds for electron occupancies of 5 down to 1. A single electron corresponds to an increased rate of about 60 Hz per channel above the -15.1 mV threshold, of which there is a background rate of about 110 Hz per channel.

The measured rates at 2400 V correspond roughly to a rate of 240 Hz per electron, about a factor of 13 lower than expected from the calculations in Section II A. This is likely due to the high threshold of 15 mV
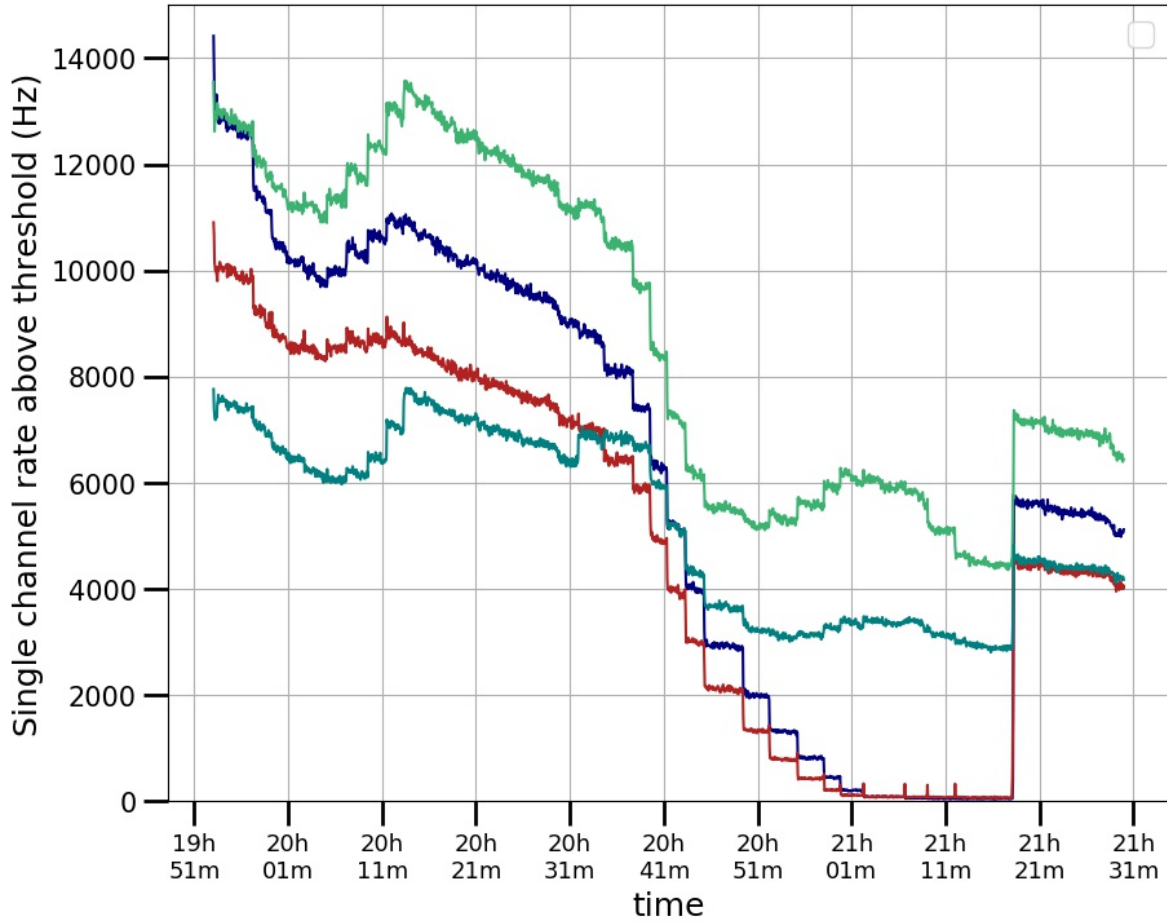
FIG. 9. Trigger rates of each anode pad as the Planacon is incrementally stepped out of the undulator radiation path. At the beginning of the time series, about 150 electrons are circulating. The detector is swept across the beam to locate the position where the rates on each channel are highest and most uniform. The final operating position is set at the end. Non-uniformities at this stage are possibly due to gain variations and non-uniform discriminator thresholds.

relative to the expected single photoelectron amplitude of about 6.6 - 8.9 mV [23].

B. Dataset description

Dataset ID	# of e-	Applied HV	Disc. Thresh.	# Events
D5	500-1000	2400 V	15.1 mV	400k
D6	0	2400 V	15.1 mV	200k
D10	1	2400 V	15.1 mV	450k
D9	0	2400 V	15.1 mV	135k
D15	1	2480 V	20.0 mV	450k
D17	0	2480 V	20.0 mV	225k

TABLE I. Datasets used in the analysis in Section VI. An increase in the high-voltage settings should increase the gain and amplitude of the single photoelectron pulses by about a factor of two.

Table I summarizes the main datasets used in the analysis stage. For most data taking sessions, the beam was
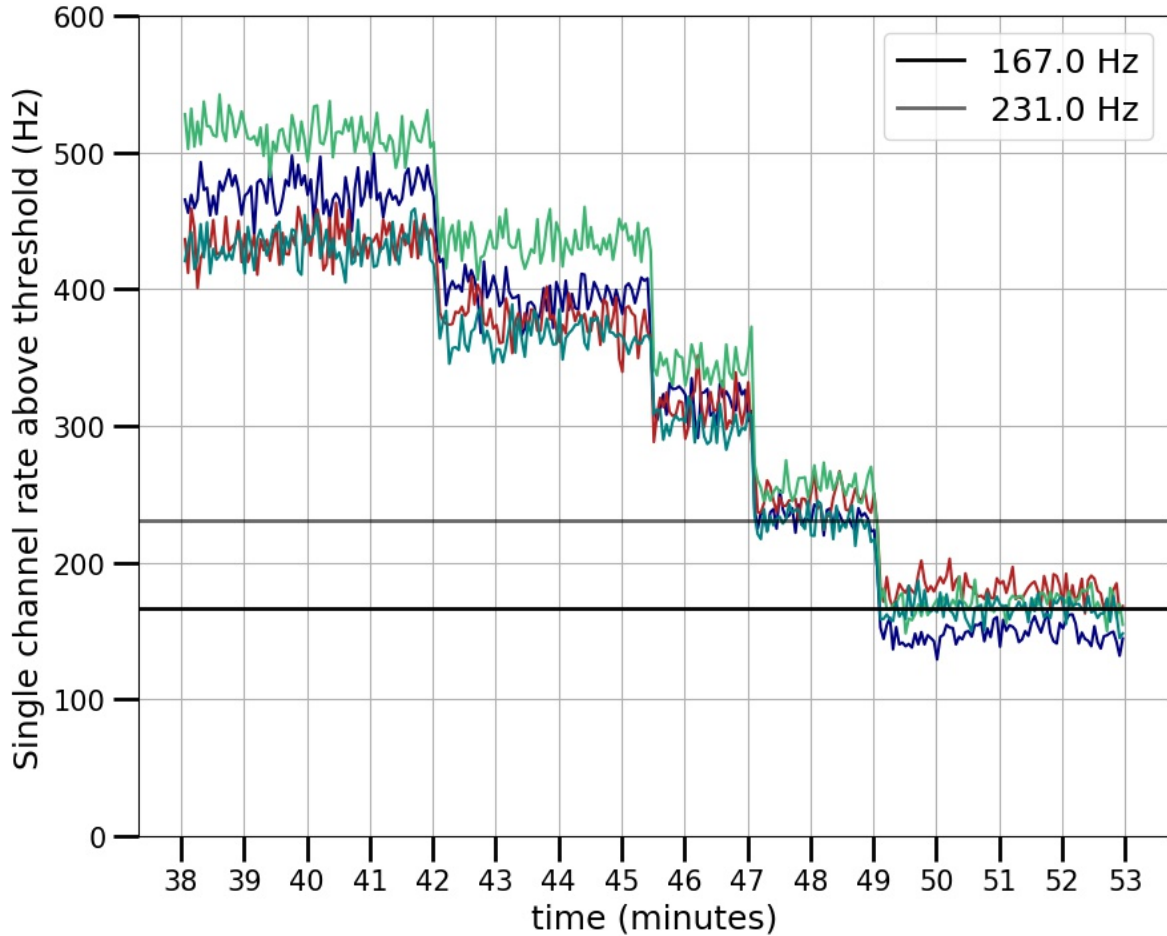
FIG. 10. Trigger rates of each anode pad as the number of electrons circulating in IOTA decreases from 5 to 1. A single electron at 2400 V input high voltage represents about 60 Hz per channel above the 15.1 mV threshold of the discriminators in this dataset. These rates represent running derivatives calculated over 3 seconds of 15 Hz sampled ACNET channels.

configured with a few hundred electrons at 100 MeV which are then scraped down to 1 electron contained within the main RF bucket that drives the gate on the discriminators. In one case, D5, data was taken with 100s of electrons in an attempt to produce a high intensity image of the undulator and dipole radiation. Immediately following or preceding each data run, a dataset was taken with all DAQ systems equivalent but with no circulating electron. These datasets represent a control dataset or "noise" dataset.

IV.   LESSONS FROM EXPERIMENTAL RUN 2B

Details of the analysis of data resulting from the datasets described in Section III are outlined in Section VI. The main lessons, or conclusions, from the experience of taking data during Run 2b is that significant improvements may be made to the measurement if one installs (1) an electronics architecture with higher signal to threshold separation and (2) finer-grained detector readout for separating the two photons in space while maintaining position resolution.

V. PROPOSED NEXT STEPS

In the next two subsections, two clear paths for a higher resolution detector configuration are described. Both paths are intended for installation within the next year (2020-2021).

A. Large Area Picosecond Photodetectors

Large Area Picosecond Photodetectors (LAPPD^{TM}) are 20×20 cm^2 active-area microchannel plate photomultipliers with quantum efficiencies on the order of 25 - 35%, single photoelectron timing resolution of 50 - 60 ps, and position resolutions on the order of 1 mm or less depending on the geometry of the readout [1–4, 21].

LAPPDs are a uniquely advantageous choice of detector for the next phase of AMPUR due to the following qualities:

- LAPPDs meet all of the AMPUR specifications in Section I C. In particular, their large area allows for a large ratio of undulator cone radius to position resolution which determines the angular correlation sensitivity.

- Multiple commercially produced LAPPDs are presently in operation at Fermilab. Fermilab has the largest number of LAPPDs in operation and testing compared to any other institution. Thus they are a familiar technology with on-site experts. There are also test facilities at Fermilab that can commission and calibrate the detectors prior to installation into IOTA.

- The capacitively coupled version of LAPPDs, often called the Generation-II LAPPDs, have a configurable readout geometry that may be changed throughout the LAPPDs lifetime for optimizing to specific measurements [3, 4, 10, 14, 15]. In other words, one may start with a phase where the readout allows for 1 mm spatial resolution over 60 electronics channels and then later move to a different readout geometry with 100 μ m resolution and 4 channels without changing the detector design.

The dark-noise rate of an MCP-PMT scales linearly with the active area, which is about 400 cm^2 for the LAPPD, which is higher compared to the $\sim$ 1 - 10 cm^2 of other commercial MCP-PMTs. Still, MCP-PMTs have much lower dark rates than some other candidate detector technologies. The total dark rate of LAPPDs is typically in the range of 1 - 10 kHz and is strongly dependent on the high voltage settings [4].

1. PSEC4 Electronics

The requirement of the electronics system for the AMPUR measurement is to determine the number of photoelectrons and their positions using the output signals from a detector. Because the expected detection rate for single and double photoelectrons is on the order of 10 kHz and 10 Hz respectively for a 7.5 MHz electron cycle frequency, the electronics system may not store signals from every turn of the electron. The electronics system may also not want to store all single photoelectron detection events.

A custom electronics system based on the fast-waveform sampling application specific integrated circuit, called the PSEC4 electronics, has been used to digitize signals from LAPPDs at Fermilab. The PSEC4 electronics system is designed to fully digitize negative polar pulses from the MCP-PMT from many readout channels to sensitively reconstruct the time-of-arrival and position of the photoelectrons. This electronics

system, described in detail in References [4] and [25], has been commissioned twice in the Fermilab Test Beam Facility (FTBF). It is presently undergoing a major firmware upgrade during the summer of 2020 that will allow it to be more applicable to the AMPUR experiment in IOTA.

In preparation for this electronics option, the Run 2b period of the AMPUR experiment used a DAQ system designed around waveform digitization and off-line reconstruction of photoelectron number and position, as outlined in Section II B. A major limiting factor in the resulting electronics system during Run 2b was the small separation of signal amplitude and trigger threshold

The PSEC4 electronics system uses on-chip constant-threshold discriminators with a minimum threshold of about 10-20 mV. Therefore, the LAPPD used must have single photoelectron amplitudes on the order of 30-40 mV (gains on the order of a few 10^7) and/or a readout with few readout conductors to increase the total parallel impedance to the digitizing electronics. Another option is to use RF amplifiers; the PSEC4 electronics board has a mezzanine connector for an optional series amplifier for each channel.

2. Strip-line anode

A primary consideration that affects the resolution of the measurement is the choice of readout geometry. The most readily available and tested readout geometry for LAPPDs is the strip-line anode. Please see References [7] and [4] for details, and Figure 11 as a photographic reference. This particular anode readout was designed to optimize timing resolution, spatial resolution, and low channel count.

While the AMPUR experiment does not rely heavily on the timing information of the detected photons, this readout geometry has been tested more than any other geometry for LAPPDs. Both the LAPPD-based time of flight (TOF) system at the FTBF and the ANNIE experiment at Fermilab uses the strip-line anode geometry. Generation-I LAPPDs sold by Incom have the strip-line anode hermetically sealed to the detector.

Typical spatial resolutions achieved for this 30-channel readout are 1 mm in both dimensions [2]. Positions may be reconstructed by either connecting digitizing electronics to both ends of each strip or connecting to only one end of each strip and measuring the delayed reflections off of unterminated ends [25].

As was seen in the four-pixel readout of the AMPUR phase of Run 2b, the size of the MCP charge-cloud relative to the readout geometry dictates the degree of signal sharing between anode pads. This plays a role in distinguishing the positions of two photons and distinguishing whether an event involves the detection of one or two photons simultaneously.

The transverse dimensions of the charge cloud from Generation-I Incom LAPPDs 42 and 43 were characterized in Reference [4]. The 9.8 ± 2.5 mm FWHM of the signal distribution on the strip-lines, in other words the transverse size of the charge cloud imaged on the strips, is reconstructed by fitting the integrated signal on each strip-line with a Gaussian. The events from this dataset are induced by cosmic ray particles that pass through a 5 mm B33 window, generating a cone of Cherenkov light with radius of about 5 mm.

3. Crossed-delay line anode

A cross delay-line anode is a readout geometry optimized for position resolution and low channel count [10, 11, 35, 36]. The cross delay line readout uses multi-layer printed circuit board (PCB) technology to create a pattern of orthogonal delay lines separated by a layer of dielectric in the PCB. The delay lines snake back and forth so that induced pulses arrive at the two ends of the delay line with a delay related to the transverse position of the MCP charge cloud. These time delays may be measured by a time-to-digital conversion circuit. Typical delays can range from 100 - 1000 ns. Position resolutions for MCP-PMTs have

FIG. 11. Photograph of the strip-line anode geometry. The anode was designed to optimize on timing resolution, spatial resolution, and low channel count. Typical spatial resolutions achieved for this 30-channel readout are 1 mm in both dimensions [2]. Typical timing resolutions for single photoelectrons are 50-70 ps.

been acheived at the level of the pore diameter, or 25 microns [35, 36].

The capacitively coupled version of LAPPDs, called the Generation-II LAPPDs, have a configurable readout geometry that may be changed throughout the LAPPDs lifetime for optimizing to specific measurements. A delay-line anode geometry has not yet been implemented as the hermetically sealed anode of a Generation-I LAPPD. On the other hand, a delay-line anode may be installed on the outside of a capacitively coupled LAPPD. Delay-line anodes for LAPPDs have not been designed or developed for use on Fermilab owned LAPPDs, though the company Incom Inc. is presently testing delay-line anode geometries.

The PSEC4 electronics have a total event-buffer length of 25 ns. Depending on the design of the delay-line anode, in particular its position resolution specification, this electronics system is not suitable due to its

limited event buffer. Crossed delay-line readouts typically have a total of four channels, which may allow for an easier search for suitable electronics systems.

B. Using multiple small MCP-PMTs with segmented anodes

Another suggested detector configuration for the next phase of the AMPUR experiment involves the use of two or more small MCP-PMTs placed adjacent to one another, each with a pixellated readout geometry similar to the one used in Run 2b or another readout geometry customized for this measurement. The use of two detectors removes the need to disambiguate overlapping MCP charge clouds shared by the relatively large anode pixels within the same detector. It may also simplify the trigger conditions for two photon events, as two pulses may either represent two coincident dark pulses, a coincident dark pulse with a single photoelectron detection, or a two photoelectron detection event where the separation angle is large enough for the photons to bridge the two detector boundaries. On the other hand, this detector configuration and its DAQ architecture must account for the possibility of completely overlapping detection of two photoelectrons.

One advantage to this detector selection is that many small area MCP-PMTs are commercially available and are widely used. The reduced area also leads to reduced dark-noise rates depending on the vendor.

C. Suggested calibration procedures

One element lacking in the preparation of the Run 2b phase of the AMPUR experiment was calibration of the detector. Only the gain was calibrated prior to installation (see Figure 6), and that calibration did not include the amplifying electronics of the data acquisition system as installed.

The following calibration procedures, assuming access to a pulsed and triggered laser system, are suggested for the next phase of this experiment:

- **Response of detector with respect to position of incident laser light**: a full 2D position scan of the detector's active area with a laser at constant intensity allows for the characterization of signal sharing and MCP charge-cloud shape for the particular detector and readout geometry used in the experiment. In other words, this is a spatial calibration of the response of multiple adjacent readout conductors to the onset of an MCP charge cloud. The 2D scan dataset may be used as a lookup table during the analysis stage. The lookup table takes an input set of signal amplitudes at each anode pixel and finds the best-matched position of either one or two coincident photoelectrons.

- **Quantum efficiency**: a careful calibration of the detector's quantum efficiency allows for the calculation of expected single and two photon event rates for a given electronics system. The quantum efficiency may be measured using a calibrated reference photodiode, a diode with adjustable but steady intensity, and an ammeter measuring the current across the gap between the photocathode and the top MCP. This measurement is possible in the Fermilab Lab 6 LAPPD test facility managed by the ANNIE experiment.

- **Single photoelectron gain**: the gain of a single photoelectron at various high voltage settings must be made in order to distinguish single and double photoelectron events. The calibration provides the best results if using the full chain of cabling and amplifiers as installed in the experiment.

VI. WAVEFORM ANALYSIS

Following a threshold crossing on any of the four Planacon readout channels in coincidence with a 20 ns beam gate aligned to the electron passage through the undulator, a trigger signal is sent to a Tektronix DPO7354 that digitizes 100 ns of waveform data on each channel. See Section II B for more details. The sampling rate of digitization is 100 ps per sample with 0.8 mV resolution.

The oscilloscope is set to record 9000 events and then save to a Tektronix ".wfm" file. The data logging process is then repeated until reaching the event counts listed in Section III. The .wfm files are reformatted for input into a Python based analysis program.

This section describes the waveform analysis methods for extracting the number of photoelectrons and their positions from the raw oscilloscope data.
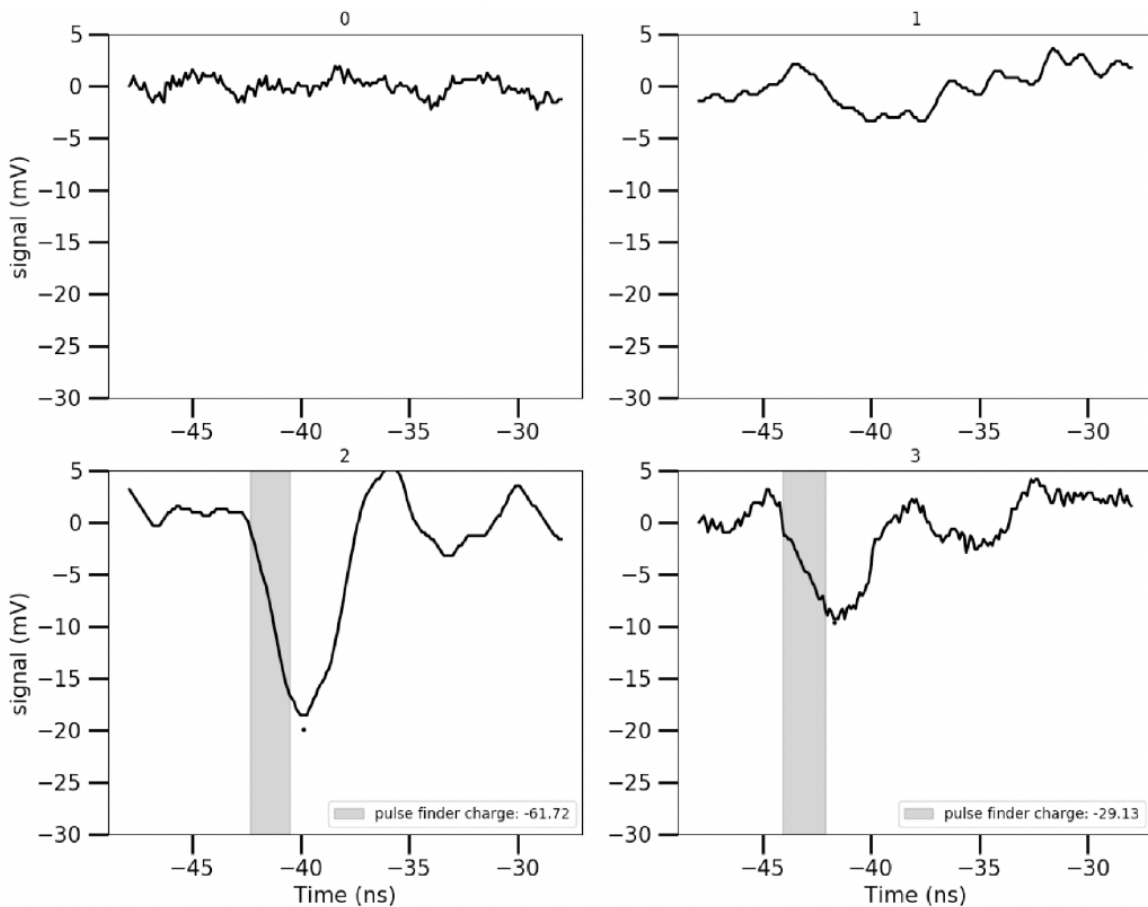

FIG. 12. An example event from dataset D10 where channel 2 has signal that passes the discriminator threshold and triggers the waveform digitizer. Channel 3 has shared some of the signal. The fractional sharing may be used to infer the position of the impinging photon or photons. Shaded regions represent the 10%-to-90% rise-time region reconstructed by the constant-fraction-discrimination analysis.

An example event is shown in Figure 12 where the photoelectron (or electrons) is primarily detected near pad 2 but has some shared signal on pad 3. Note that channels 1 and 2 have 500 MHz bandwidth where channels 0 and 3 have 3.5 GHz bandwidth due to technical complications.

The general analysis procedure goes as follows. The following subsections will expand upon these steps:

1. Perform a rough baseline subtraction by calculating the median value of all sample voltages and subtracting from all samples.

2. Trim each waveform such that only the data that aligns with the electron passage through the undulator remains. The window used is 15 ns wide. This is to reduce data processing time and data volume in the following steps. The range is set by looking at an overlay of 9000 events and centering the window on the arrival times of pulses.

3. Perform a pulse-template fitting procedure using the non-negative least squares fitting algorithm, described in detail below. The result is a noise-reduced waveform based on the expected shape of Planacon pulses.

4. Perform a pulse-property extraction routine that finds candidate pulses using a constant threshold, finds the peak of the pulse and stores the amplitude, performs a constant fraction discrimination analysis to find the 22% arrival time and other timing characteristics, and performs a rough integration over the width of the pulse.

This first pass pulse-finding analysis is used to perform more fine-tuned analysis procedures that use the coarse pulse information as an input to select golden events.

A.   Raw waveform noise reduction

A template fitting method is used to reduce noise before using a threshold discriminator to calculate properties of pulses in the event window. The template fitting method is based on the non-negative least squares (NNLS) deconvolution algorithm. For more information on the NNLS method, see References [37] and [16], Chapter 1 Section 2 of [40], and the python wrapper used in this analysis from scipy.optimize.nnls [33].

The NNLS template fit is obtained by solving the equation $\texttt{argmin}_x||\mathbf{A}\vec{x} - \vec{b}||$. In this equation, the noisy signal from front-end electronics is represented as a vector $\vec{b}$ with elements equal to the sample voltage at each time index. The jth row of the matrix $\mathbf{A}$ is a noise-less template shifted in time by j samples relative to the 0th sample of the waveform $\vec{b}$. For illustrative figures and more information, see Section 7.3.2 of Reference [4].

Because the NNLS fit is both sensitive to the template waveform shape and does not have gaussian distributed residuals, the noise-reduced waveform is not used for any other purpose than to find the rough arrival time of the peak of a pulse that crosses a constant threshold. In the case of AMPUR data, the template is formed by spline fitting (order 3) an example pulse that has been cherry picked from the data. Each channel has its own template.

B.   Pulse property extraction

Following the noise reduction procedure, the event waveforms are passed through a pulse property extraction routing with the following steps:

1. The NNLS waveform is fed into a peak finding algorithm, where every local minimum is indexed if it has a sample value lower than -6 mV and is not located within 400 ps of a nearby local minimum. This peak finding algorithm is packaged in Python by Lucas Hermann Negri as "peakutils" [24].

2. A spline fit with order 3 is performed over a 1 ns window around each peak time found in the above step. The amplitude is extracted from this spline fit.

3. The amplitude from the above step is used as input to a constant fraction discrimination function to find the 22% and 90% of amplitude time points along the rising and falling edge of the raw waveform. Linear interpolation is used to find times in between sampling intervals.

4. Only pulses with 22-to-90 risetimes between 0.2 and 5 ns are kept. This cut is performed to remove events where gross errors in the noise reduction or peak finding algorithm occurs.

5. The raw waveform is integrated from 22%-rising point to 22% falling point and stored as a rough measure of integrated signal.

The amplitude, peak time, 22% arrival time, 22-to-90 rise time, and rough integrated signal is stored for use in filtering algorithms and data analysis.
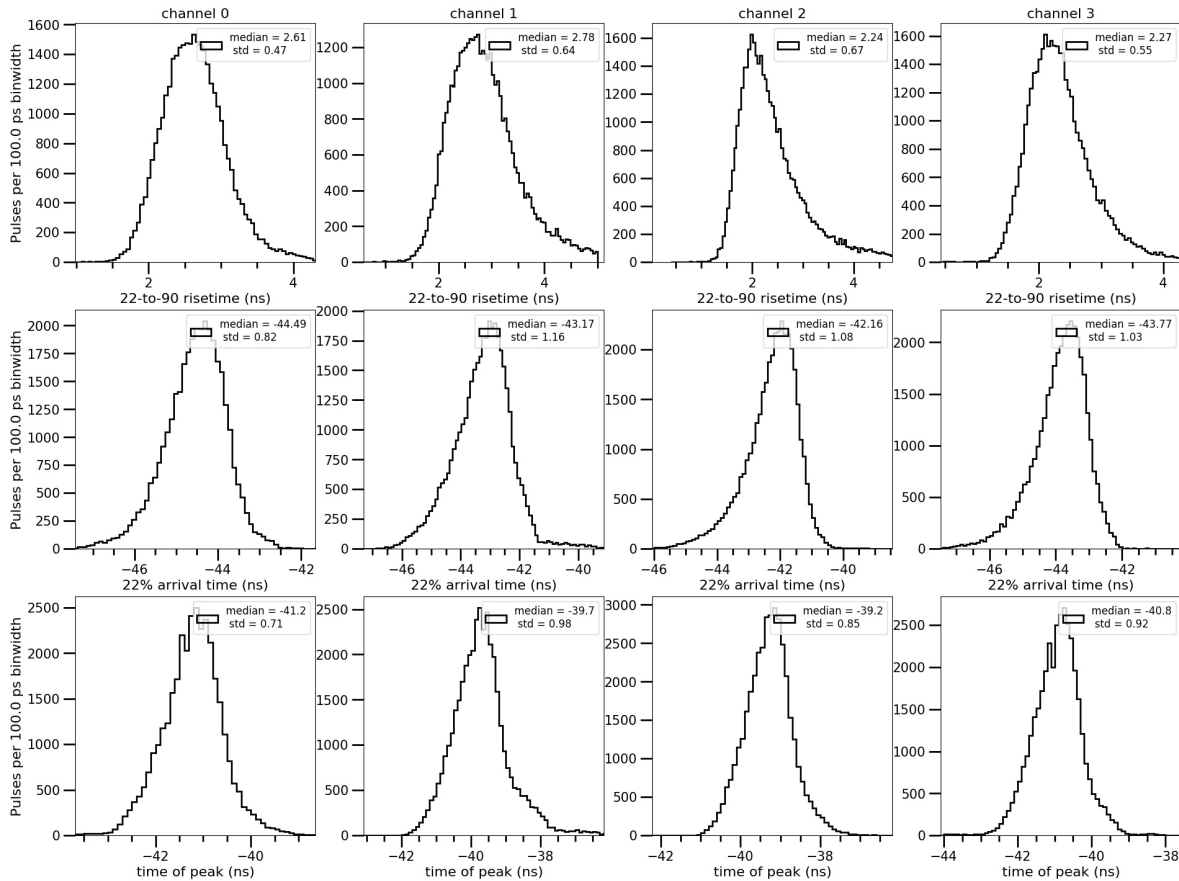
C. Timing properties of reconstructed pulses

FIG. 13. Risetime, time-of-arrival, and time-of-peak of pulses from dataset D10. The time-of-arrival is measured relative to the oscilloscope trigger, i.e. the output of the logic coincidence unit. The spread in time-of-arrival does not represent a spread of the photon arrival relative to the RF clock. The arrival times are used to identify a small arrival-time window used in off-line in the analysis.

Risetime, time-of-arrival, and time-of-peak statistics are shown in Figure 13. The spread in time-of-arrival does not represent a spread of the photon arrival relative to the RF clock, but rather the time-of-arrival relative to the oscilloscope trigger which is generated by the output of the logic coincidence unit.
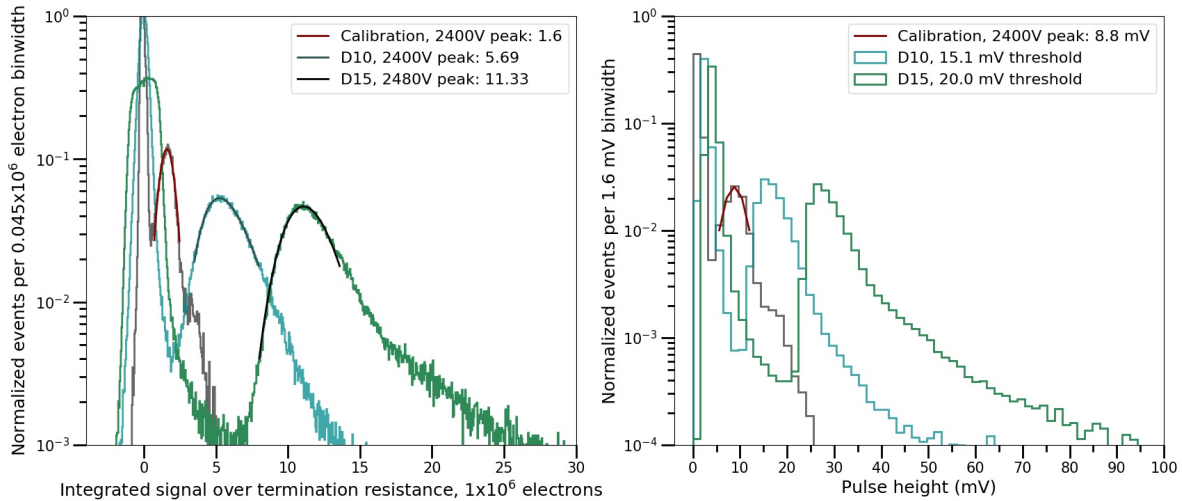
D. Spectra and thresholds

FIG. 14. The integrated signal (left) and pulse-height distributions (right) of the calibration dataset, D10, and D15 datasets. The higher amplitudes of D10 compared to the calibration dataset is due to the post-amplification NIM module. The higher amplitudes of D15 are due to the higher input high voltage, increasing the gain by about a factor of two.
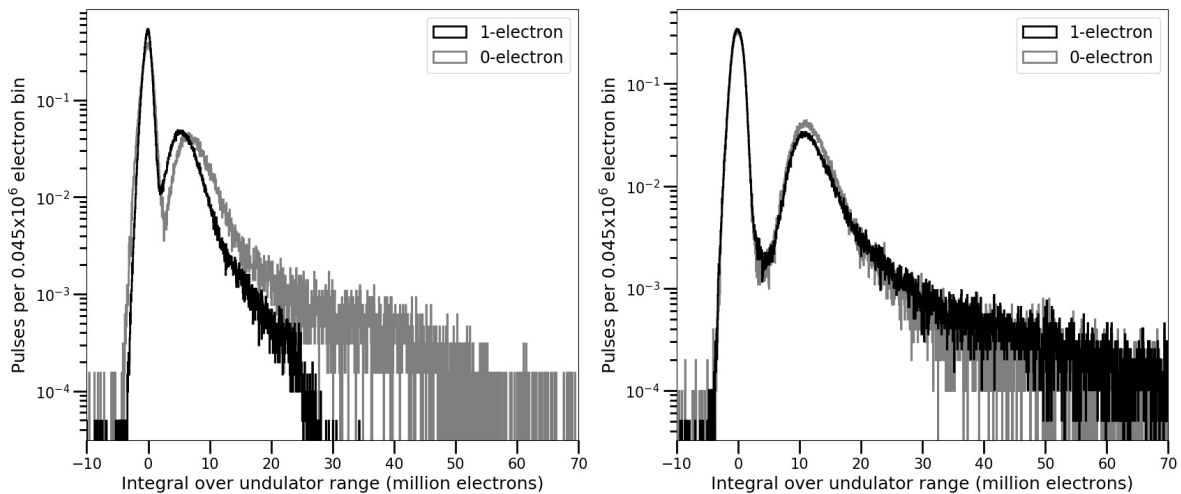
FIG. 15. Comparison between charge spectra of the 1-electron and 0-electron datasets for channel 4. Left: datasets D10 and D9 at 2400 V and 15.1 mV threshold. Right: datasets D15 and D17 with 2480 V and 20.0 mV threshold.

For all datasets, the full integral of a 10 ns wide region around the mean time-of-arrival of pulses is recorded in addition to the pulse amplitudes. As a shorthand, the integral of the waveform will be referred to as the "charge" and is divided by 50 Ω and converted to number of electrons.

The charges and pulse heights for the laser calibration dataset (no amplifiers), 2400 V dataset, and 2480 V dataset are shown in Figure 14. A lognorm distribution is fit to the charge peaks to reveal the difference in median charge between the unamplified laser calibration data and the fully cable-routed, amplified, and thresholded pulses. The increase in applied high voltage from 2400 V to 2480 V represents about a factor of 2 increase in amplitude and charge.

One takeaway from these spectra is that the voltage thresholds of the NIM discriminator for both datasets digs into the single photoelectron signal spectrum. At 2400 V, as in D10, the single photoelectron amplitude is expected to be about 6.6 mV to 8.91 mV (see Section II A) whereas the threshold is set to 15.1 mV. At 2480 V, the expected amplitude is about a factor of two higher and a 20 mV threshold was used.

During the data logging described in Section III, a so-called "noise" dataset, where 0 electrons were present in the ring, was recorded just before or after a "signal" dataset with 1 electron circulating in the ring. The charge from 2400 V and 2480 V high voltage settings is compared for both noise and signal datasets in Figure 15.

Both of these comparisons point to the need for lower dark-noise rates in the detector during the next experimental phase, as differences in these spectra are not significant. At least a factor of 2 may be achieved by reducing the beam-aligned discriminator gate from 20 ns to 10 ns.

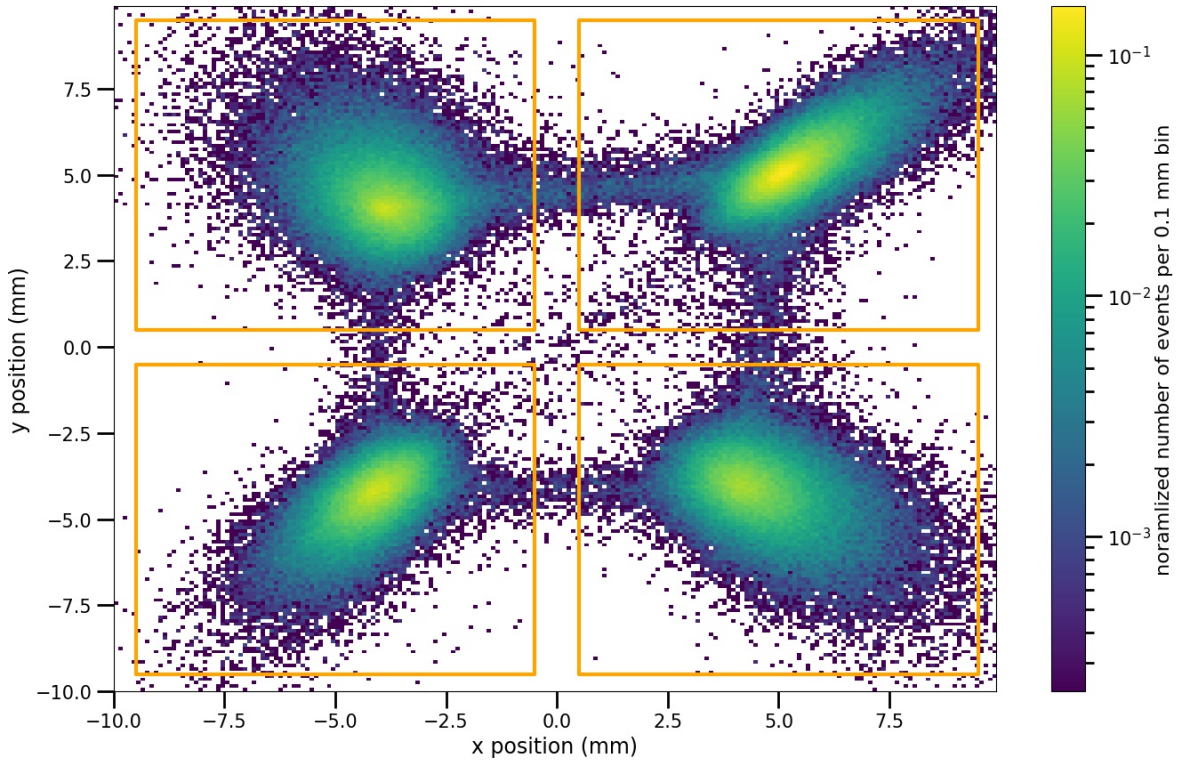## E. Position and photon-number reconstruction

FIG. 16. A histogram with log color scale of the 2D position of each event using analysis-method 1 described in the main text using dataset D15. The orange outline represents the position and boundary of the four anode pads. The color scale represents the number of events in each 0.1 mm by 0.1 mm square bin, normalized to the total number of events.

The recommended method for reconstructing the positions of all detected photoelectrons is to have a calibration dataset where a laser is scanned over the surface of the detector in many discrete steps and events are digitzed at each laser position. This forms a lookup table where the datasets at each laser position provides an average waveform for each readout conductor. For each detection in an experiment, the lookup table is searched for the laser position that has the closest matching signal distribution.

In this phase of the experiment, a finely discretized lookup-table calibration was not performed. Instead, the method of weighted mean, or "center of charge", is used to reconstruct the position of a photoelectron in an IOTA event.

If pad i at position $\vec{r}_i = (x_i, y_i)$ captures a signal intensity q_i, then the center of charge reconstruction method predicts a photoelectron position of

$$\vec{r}_{\text{reco}} = \frac{1}{\sum_i q_i} \sum_i q_i \vec{r}_i \qquad (2)$$

This equation can be further corrected by accounting for relative differences in signal response from each pad, generated from variations in gain or coupling. A calibration was performed where a laser with constant intensity was placed at the center of each anode pad and many events were digitized, shown in Figure 6. The mean amplitudes and charges from each pad's calibration dataset were recorded, resulting in relative scaling factors A_i such that

$$\vec{r}_{\text{reco}} = \frac{1}{\sum_i q_i} \sum_i (A_i/A_{\text{ref}}) q_i \vec{r}_i \tag{3}$$

where A_{ref} is the mean amplitude of one of the channels, chosen arbitrarily to be channel 1.

Two methods are used to form the signal intensities q_i:

1. Each channel's waveform is integrated over the 10 ns window described in Subsection VI D, regardless of whether a pulse exists on that channel or not. In this way, some values for q_i may be close to zero and some may have positive values due to positive pickup from electrical noise.

2. Each channel's waveform is integrated over the 10 ns window as in the first method; however, if the absolute value of the total integrated signal is not above a threshold, then that channel's q_i is set to zero. The threshold is defined as the minimum of the charge spectra, one channel shown in Figure 14, that preceeds the distribution corresponding to pulses. This method rejects signal from the electronics-noise pedestal.

Neither of these methods attempts to distinguish single photoelectron verses double photoelectron events, as a clear two photoelectron distribution is not observed in the charge spectra and a careful calibration of single photoelectron charge distribution was not performed using the full chain of cabling and amplifiers as installed in IOTA.

A 2D histogram of reconstructed positions of each event from dataset D15 are shown in Figure 16 and Figure 17 for methods 1 and 2 respectively. Most events are fully contained within a single pad, whereas some events bridge the gaps between the pads. These are events that contain significant integrated signal on multiple channels.

Figure 18 shows the difference between two histograms representing the positions of dataset D15, with 1-electron circulating the ring, and D17, with 0-electrons circulating the ring. Positive values on the color scale correspond to excess events in the 1-electron dataset relative to the 0-electron dataset. As with the charge spectrum comparison of these datasets in Figure 15, the differences in these datasets are slight. An excess of noise events in the upper-left channel could be due to the amplitude statistics of dark noise in that channel, or other effects.

VII. SUMMARY

The properties of radiation emitted when a single electron passes through an undulator element, though quantum in nature due to small occupation number, should extrapolate to the same observed properties of undulator radiation in the high occupation number of an intense electron beam. Instrumentation has been developed to view undulator radiation at single photon intensities in the Integrable Optics Test Accelerator (IOTA) at Fermilab. This document describes a first-pass installation of instrumentation for observing undulator radiation in the angular and number phase space region from a single circulating electron.

One phenomenon that is under investigation in the AMPUR experiment is a non-negligable probability of two photoelectrons being generated in a detector viewing the radiation during a single passing of the electron through the undulator. The AMPUR experiment attempted to form a picture of the angular distribution of undulator radiation during Run 2b of IOTA. The instrumentation developed may also be used to study properties of undulator radiation relevant to other applications in accelerator physics, such as optical stochastic cooling.
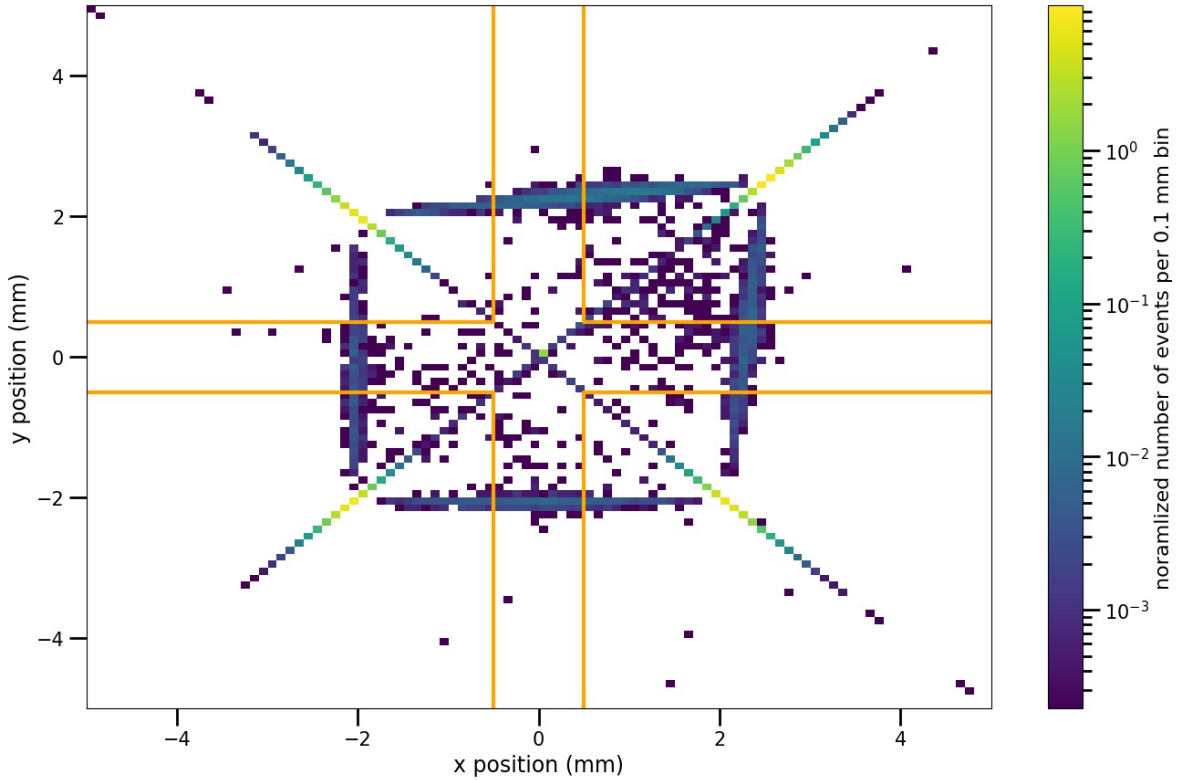
FIG. 17. A histogram with log color scale of the 2D position of each event using analysis-method 2 described in the main text using dataset D15. The x-y scale is zoomed in relative to Figure 16. The orange outline represents the position and boundary of the four anode pads. The color scale represents the number of events in each 0.1 mm by 0.1 mm square bin, normalized to the total number of events.

Experience during the AMPUR experiment, and other experiments during Run 2b, have demonstrated that attenuation of the IOTA beam to a single circulating electron may be achieved reliably on a routine basis.

Microchannel plate based photomultiplier technology is being considered as a technology for measuring the angular distribution of events where two photoelectrons are generated in a single pass of the electron. One electronics system has been tested for recording signals from a four-pixel MCP-PMT, digitizing entire waveforms while simultaneously allowing for the monitoring of the trigger rates of individual channels. The experience with this electronics system and a small, low gain MCP-PMT has lead to the following potential improvements and notes for the next phase of experimentation: (1) amplification after the detector will be needed for thresholds on the order of -10 mV and detector gains less than a few 10^7; (2) improvements to position and number reconstruction may be made if a finely discretized laser-scan calibration is provided alongside the accelerator data; (3) further reductions in detector dark noise, or a higher purity trigger condition, will provide better separation of signal to background, possibly leading to a more clear image of the angular distribution of photoelectrons.

The next phase of the AMPUR measurement, possibly called the Precision AMPUR (PAMPUR) experiment, may involve the use of either a Large Area Picosecond Photodetector (LAPPD) or multiple small commercial MCP-PMTs placed in an array. Both of these detector pathways will allow for a larger radiation-cone radius to position resolution ratio, improving the angular precision to levels on the order of 10-100 μrad. Both detector options will require the development of electronics systems that can sensitively select single photoelectron or double photoelectron events on-line during the operation of the accelerator. The route involving the use of LAPPDs could build upon the development of the PSEC4 electronics system
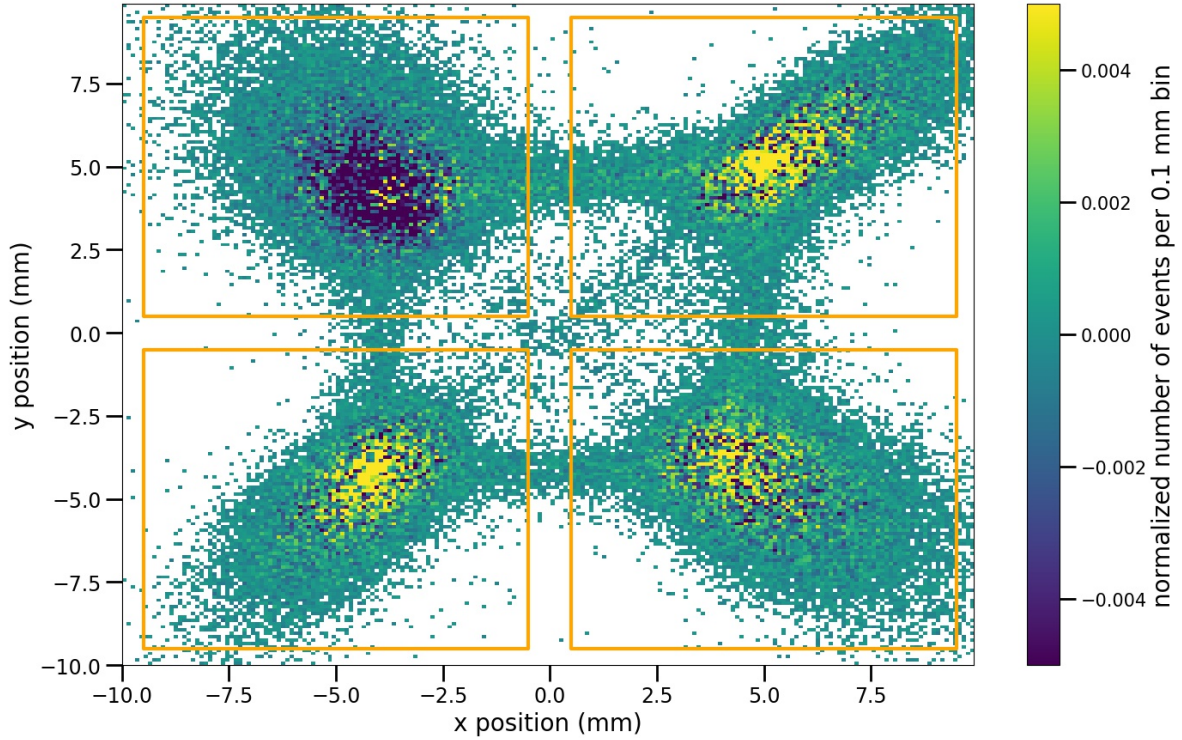
FIG. 18. The difference between 1-electron (D15) and 0-electrons (D17) position reconstruction spectrum for analysis-method 1. Positive values correspond to excess events in the 1-electron dataset compared to the 0-electron case.

used currently to digitize waveforms at high sampling rate on LAPPDs in the Fermilab Test Beam Facility time-of-flight system and the Accelerator Neutrino Neutron Interaction Experiment (ANNIE), also at Fermilab.

[1] Bernhard W. Adams, Klaus Attenkofer, Mircea Bogdan, Karen Byrum, Andrey Elagin, Jeffrey W. Elam, Henry J. Frisch, Jean-Francois Genat, Herve Grabas, Joseph Gregar, Elaine Hahn, Mary Heintz, Zinetula Insepov, Valentin Ivanov, Sharon Jelinsky, Slade Jokely, Sun Wu Lee, Anil. U. Mane, Jason McPhate, Michael J. Minot, Pavel Murat, Kurtis Nishimura, Richard Northrop, Razib Obaid, Eric Oberla, Erik Ramberg, Anatoly Ronzhin, Oswald H. Siegmund, Gregory Sellberg, Neal T. Sullivan, Anton Tremsin, Gary Varner, Igor Veryovkin, Alexei Vostrikov, Robert G. Wagner, Dean Walters, Hsien-Hau Wang, Matthew Wetstein, Junqi Xi, Zikri Yusov, and Alexander Zinovev. A brief technical history of the large-area picosecond photodetector (lappd) collaboration, 2016.

[2] B.W. Adams, A. Elagin, H.J. Frisch, R. Obaid, E. Oberla, A. Vostrikov, R.G. Wagner, J. Wang, and M. Wetstein. Timing characteristics of large area picosecond photodetectors. *Nuclear Instruments and Methods in Physics Research Section A: Accelerators, Spectrometers, Detectors and Associated Equipment*, 795:1 – 11, 2015.

[3] E. Angelico, T. Seiss, B. Adams, A. Elagin, H. Frisch, and E. Spieglan. Capacitively coupled pickup in mcp-based photodetectors using a conductive metallic anode. *Nuclear Instruments and Methods in Physics Research Section A: Accelerators, Spectrometers, Detectors and Associated Equipment*, 846:75 – 80, 2017.

[4] Evan Angelico. Development of large-area mcp-pmt photo-detectors for a precision time-of-flight system at the fermilab test beam facility. *Fermilab Technical Documents*, 1 2020.

[5] S. Antipov, D. Broemmelsiek, D. Bruhwiler, D. Edstrom, E. Harms, V. Lebedev, J. Leibfritz, S. Nagaitsev, C.S. Park, H. Piekarz, P. Piot, E. Prebys, A. Romanov, J. Ruan, T. Sen, G. Stancari, C. Thangaraj, R. Thurman-Keup, A. Valishev, and V. Shiltsev. IOTA (integrable optics test accelerator): facility and experimental beam physics program. *Journal of Instrumentation*, 12(03):T03002–T03002, mar 2017.

[6] Roy Glauber. Coherent and incoherent states of the radiation field. *Phys. Rev. Letters*, 131, 1963.

[7] HervÃľ Grabas, Razib Obaid, Eric Oberla, Henry Frisch, Jean-Francois Genat, Richard Northrop, Fukun Tang, David McGinnis, Bernhard Adams, and Matthew Wetstein. Rf strip-line anodes for psec large-area mcp-based photodetectors. *Nuclear Instruments and Methods in Physics Research Section A: Accelerators, Spectrometers, Detectors and Associated Equipment*, 711:124 – 131, 2013.

[8] Aliaksei Halavanau, Zhirong Huang, Ihar Lobach, Sergei Nagaitsev, Claudio Pellegrini, Tor Raubenheimer, and Daniel Seipt. Undulator Radiation Generated by a Single Electron. In *10th International Particle Accelerator Conference*, page TUPRB089, 2019.

[9] M. R. Howells. *The Properties of Undulator Radiation*. 1992. NATO Advanced Study Institute, Maratea, Italy, June 28 - July 10, 1992.

[10] O. Jagutzki, A. Czasch, and S. SchÃűssler. Performance of a compact position-sensitive photon counting detector with image charge coupling to an air-side anode. *Proc. SPIE*, 8727:87270T–87270T–12, 2013.

[11] Ottmar Jagutzki et al. Fast-position and time-sensitive readout of image intensifiers for single-photon detection. *Proc. SPIE*, 3764:61–69, 1999.

[12] Kwang-Je Kim. Quantum fluctuations in beam dynamics. Presented at the 15th ICFA Advanced Beam Dynamics Workshop on Quantum Aspects of Beam Physics, 1998.

[13] KwangâĂŘJe Kim. Characteristics of synchrotron radiation. *AIP Conference Proceedings*, 184(1):565–632, 1989.

[14] J. S. Lapington, J. R. Howorth, and J. S. Milnes. A reconfigurable image tube using an external electronic image readout. *Proc. SPIE*, 5881:588109–588109–10, 2005.

[15] J. S. Lapington, J. R. Howorth, and J. S. Milnes. Demountable readout technologies for optical image intensifiers. *NIM A*, 573:243–246, 2007.

[16] Charles L. Lawson and Richard J. Hanson. *Solving Least Squares Problems*. Society for Industrial and Applied Mathematics, 1995.

[17] I. Lobach et al. Study of Fluctuations in Undulator Radiation in the IOTA Ring at Fermilab. In *Proc. 10th International Particle Accelerator Conference (IPAC'19), Melbourne, Australia, 19-24 May 2019*, number 10 in International Particle Accelerator Conference, pages 777–780, Geneva, Switzerland, Jun. 2019. JACoW Publishing. https://doi.org/10.18429/JACoW-IPAC2019-MOPRB088.

[18] Ihar Lobach. Wigrad simulation wrapper for the slac sti optronics undulator. https://github.com/IharLobach/wigrad.

[19] Ihar Lobach, Valeri Lebedev, Sergei Nagaitsev, Aleksandr Romanov, Giulio Stancari, Alexander Valishev, Aliaksei Halavanau, Zhirong Huang, and Kwang-Je Kim. Statistical properties of spontaneous synchrotron radiation

with arbitrary degree of coherence. *Phys. Rev. Accel. Beams*, 23:090703, Sep 2020.

[20] Ihar Lobach, Valeri Lebedev, Sergei Nagaitsev, Aleksandr Romanov, Giulio Stancari, Alexander Valishev, Aliaksei Halavanau, Zhirong Huang, and Kwang-Je Kim. Statistical properties of spontaneous synchrotron radiation with arbitrary degree of coherence. *Phys. Rev. Accel. Beams*, 23:090703, Sep 2020.

[21] A.V. Lyashenko, B.W. Adams, M. Aviles, T. Cremer, C.D. Ertley, M.R. Foley, M.J. Minot, M.A. Popecki, M.E. Stochaj, W.A. Worstell, and et al. Performance of large area picosecond photo-detectors (lappdtm). *Nuclear Instruments and Methods in Physics Research Section A: Accelerators, Spectrometers, Detectors and Associated Equipment*, 958:162834, 4 2020.

[22] The NIM disciminator used is a model 710D octal discriminator from Fermilab PREP services. This discriminator has a -10 mV minimum threshold. During this experiment, these thresholds were found to drift by up to 2 - 5 mV over a period of 30 minutes. At -15 mV, stability was much better. This document refers to -15 mV as the minimum threshold.

[23] All thresholds and amplitudes are negative relative to the common ground. Sometimes the negative sign is omitted in the text and plots.

[24] Peakutils python package: https://peakutils.readthedocs.io/en/latest/.

[25] Eric Oberla. *Charged particle tracking in a water Cherenkov optical time projection chamber*. PhD thesis, University of Chicago, 2015. Copyright - Database copyright ProQuest LLC; ProQuest does not claim copyright in the individual underlying works; Last updated - 2020-02-07.

[26] I. Ostrovskiy, F. Retiere, D. Auty, J. Dalmasson, T. Didberidze, R. DeVoe, G. Gratta, L. Huth, L. James, L. Lupin-Jimenez, N. Ohmart, and A. Piepke. Characterization of silicon photomultipliers for nexo. *IEEE Transactions on Nuclear Science*, 62(4):1825–1836, 2015.

[27] Jinseo Park, Fangjian Wu, Evan Angelico, Henry J. Frisch, and Eric Spieglan. Segmented anodes with sub-millimeter spatial resolution for mcp-based photodetectors, 2020.

[28] Photonis. Photon detector xpm85112 miniplanacon. https://cdcvs.fnal.gov/redmine/attachments/60308/Photonis_miniPLANACON_4x4_XPM85112_datasheet.pdf. Datasheet from the manufacturer.

[29] Photonis. Planacon. https://www.photonis.com/products/planacon.

[30] Photonis. Test sheet for iota miniplanacon xpm85112. https://cdcvs.fnal.gov/redmine/attachments/60307/Photonis_XPM85112_9002009_test_data.pdf.

[31] RFElectronik. Coaxial cable attenuation charts. http://rfelektronik.se/manuals/Datasheets/Coaxial_Cable_Attenuation_Chart.pdf.

[32] Schott. Schott borofloat 33. Brochure.

[33] scipy. scipy.optimize.nnls fortran wrapper for the nnls solver. https://docs.scipy.org/doc/scipy/reference/generated/scipy.optimize.nnls.html, 2019.

[34] sensL. An introduction to the silicon photomultiplier. https://www.sensl.com/downloads/ds/TN-IntrotoSPMTech.pdf. Technical note.

[35] O. Siegmund, J. Vallerga, P. Jelinsky, X. Michalet, and S. Weiss. Cross delay line detectors for high time resolution astronomical polarimetry and biological fluorescence imaging. In *IEEE Nuclear Science Symposium Conference Record, 2005*, volume 1, pages 448–452, 2005.

[36] Oswald H. W. Siegmund, John V. Vallerga, Barry Y. Welsh, Jason McPhate, Michael W. Rabin, and Jeffrey J. Bloch. Advanced photon counting imaging detectors with 100ps timing for astronomical and space sensing applications. 2006.

[37] Martin Slawski and Matthias Hein. Non-negative least squares for high-dimensional linear models: consistency and sparse recovery without regularization, 2012.

[38] ThorLabs. Thorlabs bb2-e02 fused silica broadband dielectric mirror. https://www.thorlabs.com/newgrouppage9.cfm?objectgroup_id=139&pn=BB2-E02.

[39] Joseph Ladislas Wiza. Microchannel plate detectors. *Nuclear Instruments and Methods*, 162:587–601, 1979.

[40] Jiaying Wu. *A Signal Processing Approach for Preprocessing and 3d Analysis of Airborne Small-Footprint Full Waveform Lidar Data*. PhD thesis, 2012.